On the Reliability of Magnetic Energy and Helicity Computations Based on Nonlinear Force-free Coronal Magnetic Field Models

Julia K. Thalmann[1] , L. Linan[2], E. Pariat[2] , and G. Valori[3]
[1] University of Graz, Institute of Physics/IGAM, Universitätsplatz 5, A-8010 Graz, Austria; julia.thalmann@uni-graz.at
[2] LESIA, Observatoire de Paris, Université PSL, CNRS, Sorbonne Université, Université de Paris, 5 place Jules Janssen, F-92195 Meudon, France
[3] Mullard Space Science Laboratory, University College London, Holmbury St. Mary, Dorking, Surrey RH5 6NT, UK
Received 2019 June 17; revised 2019 July 1; accepted 2019 July 2; published 2019 July 18

Abstract

We demonstrate the sensitivity of magnetic energy and helicity computations regarding the quality of the underlying coronal magnetic field model. We apply the method of Wiegelmann & Inhester to a series of *Solar Dynamics Observatory*/Helioseismic and Magnetic Imager vector magnetograms, and discuss nonlinear force-free (NLFF) solutions based on two different sets of the free model parameters. The two time series differ from each other concerning their force-free and solenoidal quality. Both force- and divergence-freeness are required for a consistent NLFF solution. Full satisfaction of the solenoidal property is inherent in the definition of relative magnetic helicity in order to ensure gauge independence. We apply two different magnetic helicity computation methods to both NLFF time series and find that the output is highly dependent on the level to which the NLFF magnetic fields satisfy the divergence-free condition, with the computed magnetic energy being less sensitive than the relative helicity. Proxies for the nonpotentiality and eruptivity derived from both quantities are also shown to depend strongly on the solenoidal property of the NLFF fields. As a reference for future applications, we provide quantitative thresholds for the force- and divergence-freeness, for the assurance of reliable computation of magnetic energy and helicity, and of their related eruptivity proxies.

Key words: methods: data analysis – methods: numerical

1. Introduction

For practical cases, Valori et al. (2012) demonstrated the validity and physical meaningfulness to compute (and track in time) the relative magnetic helicity in order to characterize (the evolution of) a magnetic system. As its name implies, the relative helicity allows it to express the helicity of a magnetic field with respect to a reference field. This relative formulation allows it to circumvent the problem that magnetic helicity cannot be defined meaningfully for systems that are not magnetically closed (such as the solar corona).

Following Berger & Field (1984) and Finn & Antonsen (1984), the relative magnetic helicity (simply called helicity hereafter) in a volume, $\mathcal{V}$, bounded by a surface, $\partial\mathcal{V}$, can be written as

$$H_\mathcal{V} = \int_\mathcal{V} (\boldsymbol{A} + \boldsymbol{A}_\mathrm{p}) \cdot (\boldsymbol{B} - \boldsymbol{B}_0) \, d\mathcal{V}, \qquad (1)$$

where the reference field, $\boldsymbol{B}_0$, shares the normal component of the studied field $\boldsymbol{B}$ on $\partial\mathcal{V}$. Often, a potential (current-free) field is used as reference field (see Prior & Yeates 2014 for an alternative choice). In Equation (1), $\boldsymbol{A}$ and $\boldsymbol{A}_\mathrm{p}$ are the vector potentials satisfying $\boldsymbol{B} = \nabla \times \boldsymbol{A}$ and $\boldsymbol{B}_0 = \nabla \times \boldsymbol{A}_\mathrm{p}$, respectively.

Following Berger (1999), Equation (1) may be written as $H_\mathcal{V} = H_\mathrm{J} + H_\mathrm{PJ}$, with

$$H_\mathrm{J} = \int_\mathcal{V} (\boldsymbol{A} - \boldsymbol{A}_\mathrm{p}) \cdot (\boldsymbol{B} - \boldsymbol{B}_0) \, d\mathcal{V}, \qquad (2)$$

$$H_\mathrm{PJ} = 2 \int_\mathcal{V} \boldsymbol{A}_\mathrm{p} \cdot (\boldsymbol{B} - \boldsymbol{B}_0) \, d\mathcal{V}. \qquad (3)$$

Here, H_J is the magnetic helicity in the volume associated with the electric current, and H_PJ is the helicity associated with the component of the field that is threading $\partial\mathcal{V}$. Because $\boldsymbol{B}$ and $\boldsymbol{B}_0$ are designed such that they share their normal component, $\boldsymbol{B}_n$, on $\partial\mathcal{V}$, not only $H_\mathcal{V}$ but also both H_J and H_PJ are independently gauge invariant.

Importantly, the underlying magnetic fields, $\boldsymbol{B}$ and $\boldsymbol{B}_0$, have to adhere to a certain level of divergence-freeness, in order to ensure reliable helicity computation. For this purpose, Valori et al. (2013) used the decomposition of the magnetic energy within $\mathcal{V}$ in the form

$$E = \frac{1}{2\mu_0} \int_\mathcal{V} B^2 \, d\mathcal{V} = E_0 + E_\mathrm{J}$$
$$= E_{0,\mathrm{s}} + E_{\mathrm{J},\mathrm{s}} + E_{0,\mathrm{ns}} + E_{\mathrm{J},\mathrm{ns}} + E_\mathrm{mix}, \qquad (4)$$

with E_0 and E_J being the energies of the potential and current-carrying magnetic field, respectively. E_0 is used to compute an upper limit for the free energy as $E_\mathrm{F} = E - E_0$. $E_{0,\mathrm{s}}$ and $E_{\mathrm{J},\mathrm{s}}$ are the energies of the potential and current-carrying solenoidal magnetic field components. $E_{0,\mathrm{ns}}$ and $E_{\mathrm{J},\mathrm{ns}}$ are those of the corresponding nonsolenoidal components. E_mix corresponds to all cross terms (see Equation (8) in Valori et al. 2013 for the detailed expressions). For a perfectly solenoidal field, one finds $E_{0,\mathrm{s}} = E_0$, $E_{\mathrm{J},\mathrm{s}} = E_\mathrm{J}$, and $E_{0,\mathrm{ns}} = E_{\mathrm{J},\mathrm{ns}} = E_\mathrm{mix} = 0$.

Based on Equation (4), Valori et al. (2016) introduced the ratio E_div/E, with $E_\mathrm{div} = E_{0,\mathrm{ns}} + E_{\mathrm{J},\mathrm{ns}} + |E_\mathrm{mix}|$, as to be indicative of the divergence-freeness of the magnetic field, and tested the corresponding sensitivity of Equation (1), based on different numerical methods to compute magnetic helicity. Based on a specifically designed numerical experiment, where a finite divergence was added in a controlled way to a numerically solenoidal MHD model case, it was shown that the error in the computation of $H_\mathcal{V}$ may grow considerably if $E_\mathrm{div}/E \gtrsim 0.1$.

Magnetic helicity computations are often performed based on nonlinear force-free (NLFF) coronal magnetic field extrapolations, using the optimization method of Wiegelmann & Inhester (2010). It represents the numerical solution to the boundary value problem of extrapolation of the measured surface magnetic field into the solar corona:

$$(\nabla \times \boldsymbol{B}) \times \boldsymbol{B} = \boldsymbol{0}, \quad (5)$$

$$\nabla \cdot \boldsymbol{B} = 0. \quad (6)$$

The method allows several free model parameters to be chosen, in order to optimize the numerical solution of Equations (5) and (6). If used as a black box, predefined values are used, without optimization regarding underlying specific magnetogram data. The predefined values are to be thought of as to be initial guesses only, however, and a careful testing and tuning of the free model parameters is inevitable. Only a careful selection of the free model parameters is capable of producing NLFF solutions of highest quality, both in terms of force- and divergence-freeness. A high degree of force-freeness is crucial for the validity of the NLFF solution with respect to the measured photospheric field it is based on. A low level of divergence is mandatory for a reliable computation of $H_{\mathcal{V}}$.

The presented work represents an extension of the work by Valori et al. (2016), by considering the dependency of energy and helicity computations on the field's solenoidal property in observed solar cases, rather than an idealized model. Our work shall serve as a reference, concerning the quality an NLFF model has to suffice, in order to be used as an input for reliable helicity modeling.

2. Method

We use photospheric vector magnetic field data (Hoeksema et al. 2014), derived from *Solar Dynamics Observatory* (*SDO*; Pesnell et al. 2012) Helioseismic and Magnetic Imager (HMI; Schou et al. 2012) polarization measurements. We use the HMI.SHARP_CEA_720S data series that provides a Lambert Cylindrical Equal-Area projected magnetic field vector within automatically identified active region patches (Bobra et al. 2014), with the azimuthal component of the vector magnetic field being disambiguated (Metcalf 1994; Leka et al. 2009).

For computational feasibility, we bin the photospheric data by a factor of 4 to a plate scale of $0°.12$. We set our analysis time range such that it covers the time period 2011 February 12–16, i.e., the disk passage of active region (AR) NOAA 11158. Around intense flares (equal or larger *GOES* class M5.0), we use HMI's native time cadence of 12 minutes, and a 1 hr cadence otherwise.

Based on the binned vector magnetic field data, we compute NLFF equilibria for each time step, which involves two computational steps. First, we "preprocess" the data, to obtain a more force-free consistent state (Wiegelmann et al. 2006). The preprocessing method allows different free parameters to be set:

1. μ_1 and μ_2 control the level of force and torque of the data;
2. μ_3 allows deviations from the input data; and
3. μ_4 controls the degree of applied smoothing.

In the original notation the predefined standard setting is (μ_1, μ_2, μ_3, μ_4) = (1 ,1, 10^{-3}, 10^{-2}).

Second, we apply the method of Wiegelmann & Inhester (2010) to the preprocessed maps. The optimization approach is designed such that the functional

$$L = \int_V w_f \frac{|(\nabla \times \boldsymbol{B}) \times \boldsymbol{B}|^2}{B^2} + w_d \, |\nabla \cdot \boldsymbol{B}|^2 \, dv$$
$$+ \nu \int_S (\boldsymbol{B} - \boldsymbol{B}_{\mathrm{obs}}) \cdot \boldsymbol{W} \cdot (\boldsymbol{B} - \boldsymbol{B}_{\mathrm{obs}}) ds \quad (7)$$

is minimized such that the volume-integrated Lorentz force and divergence becomes small.

The surface term in Equation (7) allows deviations between the NLFF solution, $\boldsymbol{B}$, and the magnetic field information at the lower boundary, $\boldsymbol{B}_{\mathrm{obs}}$, in order to find a more force-free solution. The deviation from $\boldsymbol{B}_{\mathrm{obs}}$ is controlled by the diagonal error matrix, $\boldsymbol{W}$, which allows it to incorporate uncertainties on each component of the magnetic field, and in each pixel, separately. Ideally, $\boldsymbol{B}_{\mathrm{obs}}$ would be a magnetogram measured at a chromospheric height, i.e., in a force-free regime of the solar atmosphere. In practice, the preprocessed photospheric vector field, $\boldsymbol{B}_{\mathrm{pp}}$, is supplied so that $\boldsymbol{B}_{\mathrm{obs}} = \boldsymbol{B}_{\mathrm{pp}}$.

The model parameters that can be freely assigned in Equation (7) are:

1. Separate weightings of the volume-integrated force (w_f) and divergence (w_d). In the original notation these are set as $w_f = w_d = 1$.
2. The components w_{los} and w_{hor} of the diagonal error matrix, $\boldsymbol{W}$, can be defined in different ways. The choice $w_{\mathrm{los}} = w_{\mathrm{hor}} = 1$ assures accuracy of both the longitudinal and horizontal magnetic field equally at all pixel locations. Alternatively, $w_{\mathrm{hor}} = |B_{\mathrm{hor}}|/\max(|B_{\mathrm{hor}}|)$ may be applied, i.e., assuming stronger horizontal fields to be measured with higher accuracy.
3. The impact of the surface term, i.e., the influence of $\boldsymbol{B}_{\mathrm{obs}}$ onto the final NLFF solution, is controlled by ν. Wiegelmann & Inhester (2010) suggest ν in the range 10^{-4}–10^{-1}.

Successful NLFF modeling involves finding a combination of free model parameters that delivers optimized results, in terms of force- and divergence-freeness. In order to quantify the consistency of the obtained NLFF solutions, we use the current-weighted average of the angle between the modeled magnetic field and electric current density, θ_J (Schrijver et al. 2006). We use the volume-averaged fractional flux, $\langle|f_i|\rangle$ (Wheatland et al. 2000), and the energy ratio, E_{div}/E (Valori et al. 2013), to quantify the level of divergence of the NLFF solution.

We use two finite-volume (FV) methods to compute the magnetic helicity based on Equations (1)–(3). The method of Thalmann et al. (2011) solves systems of partial differential equations to obtain the vector potentials $\boldsymbol{A}$ and $\boldsymbol{A}_{\mathrm{p}}$, using the Coulomb gauge, $\nabla \cdot \boldsymbol{A} = \nabla \cdot \boldsymbol{A}_{\mathrm{p}} = 0$ ("FV$_{\mathrm{Coulomb}}$" hereafter). The method of Valori et al. (2012) is based on integral formulations, using the DeVore gauge, $A_z = A_{\mathrm{p},z} = 0$ ("FV$_{\mathrm{DeVore}}$" hereafter). Both methods define the reference field as $\boldsymbol{B}_0 = \nabla\phi$, with ϕ being the scalar potential, subject to the constraint $\nabla_n\phi = \boldsymbol{B}_n$ on $\partial\mathcal{V}$. The methods have been tested in the framework of an extended proof-of-concept study on FV helicity computation methods (Valori et al. 2016), where it has been shown that for various test setups the methods deliver helicity values in line with each other, differing by a few percent only.
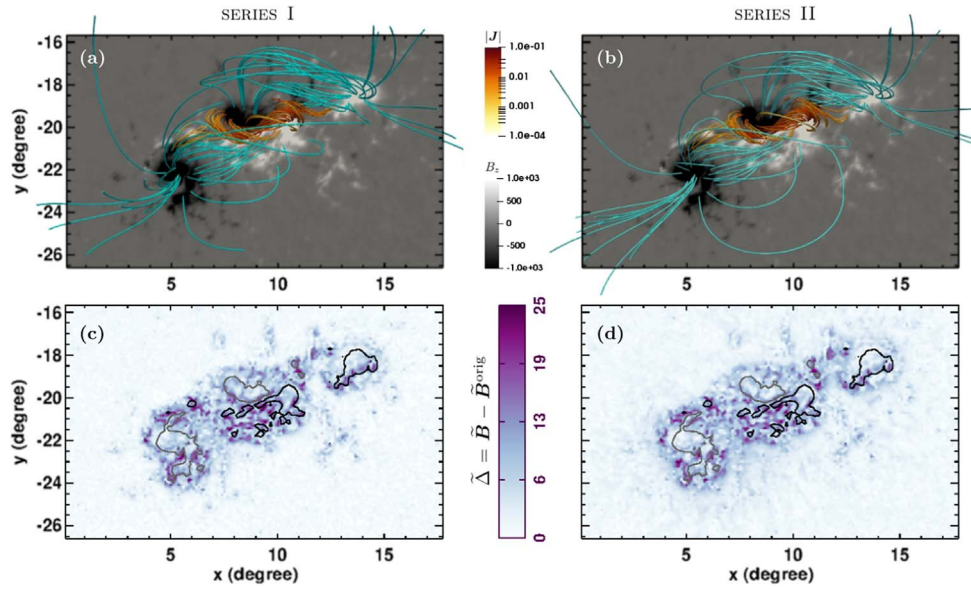
Figure 1. NLFF model solution for February 14 at 21:00 UT in (a) SERIES I and (b) SERIES II. Sample field lines outlining the large-scale magnetic field are colored green. Those originating from the AR center are color-coded according to the total absolute current density, $|J|$, at their footpoints. The gray scale background shows the measured vertical magnetic field, B_z, scaled to ± 1 kG. Panels (c) and (d) show the respective normalized changes at the lower NLFF boundary. Black/gray contours are drawn at ± 750 G.

In total we employed 18 NLFF extrapolations of the same HMI magnetogram at 12:00 UT, obtained with 18 different combinations of the parameters (μ_3, μ_4, w_d, $w_{\rm hor}$), in order to pin down successful parameter sets. Unphysical NLFF solutions with $E_0 < E$ and solutions where $E_{\rm div}/E > 0.1$ were discarded from further consideration. Seven solutions were found with favorable properties for helicity modeling, with $E_{\rm div}/E \lesssim 0.1$. Out of those, two parameter sets were chosen for further consideration. In combination with (μ_1, μ_2, w_f, ν) = (1, 1, 1, 10^{-3}), our first selected choice (μ_3, μ_4, w_d, $w_{\rm hor}$) = (10^{-3}, 10^{-3}, 2, $\propto B_{\rm hor}$) delivered an NLFF solution with an exceptionally low solenoidal level ($E_{\rm div}/E < 0.01$). An NLFF model solution close to the limit $E_{\rm div}/E \simeq 0.1$, suggested as to be tolerable for helicity modeling in Valori et al. (2016), was found based on the choice (μ_3, μ_4, w_d, $w_{\rm hor}$) = (10^{-3}, 10^{-3}, 1, 1), and also selected for further analysis.

We used these two sets of free model parameters to compute the full time series of NLFF models for NOAA 11158 between February 12 00:00 UT and February 16 00:00 UT (hereafter called SERIES II and SERIES I respectively), in order to demonstrate how important the degree of $\nabla \cdot \boldsymbol{B}$ of the input NLFF solutions is for successful helicity computation.

3. Results

3.1. Properties and Quality of NLFF Modeling

In Figures 1(a) and (b), the NLFF model solution of SERIES I and SERIES II for February 14 21:00 UT are shown, respectively. Both reveal a low-lying system of helical magnetic field along the main polarity inversion line in the AR center, in agreement with earlier works (e.g., Jing et al. 2012; Sun et al. 2012; Inoue et al. 2013).

Based on the used free parameter sets, the binned vector magnetic field, $\boldsymbol{B}^{\rm orig}$, is changed to a different degree during NLFF modeling. Following DeRosa et al. (2015), we characterize the modifications of the vector field at the lower

Table 1
Changes to the Measured Magnetic Field during NLFF Modeling, as Shown in Figures 1(c) and (d)

Series	$\Delta_z^{\rm rms}$ (G)	$\Delta_h^{\rm rms}$ (G)	$\widetilde{\Delta}_z^{\rm rms}$ (G)	$\widetilde{\Delta}_h^{\rm rms}$ (G)
I	68.74	181.36	4.30	2.42
II	63.03	103.54	4.06	2.88

boundary ($z = 0$) as

$$\Delta = \boldsymbol{B}_i - \boldsymbol{B}_i^{\rm orig} \qquad (8)$$

for each component $i = \{x, y, z\}$, where $\boldsymbol{B}$ is the final magnetic field at the lower boundary of the NLFF model. The magnitudes of the changes are considered separately for the vertical (Δ_z) and horizontal magnetic field $\Delta_h = |(\Delta_x, \Delta_y)|$. In addition, we use the normalized change, $\widetilde{\Delta} = \widetilde{\boldsymbol{B}} - \widetilde{\boldsymbol{B}}^{\rm orig}$, to incorporate the measurement uncertainties for each component, σ_i, where $\widetilde{B}_i = B_i/\sigma_i$ and $\widetilde{B}_i^{\rm orig} = B_i^{\rm orig}/\sigma_i$, for the computation of $\widetilde{\Delta}_z$ and $\widetilde{\Delta}_h = |(\widetilde{\Delta}_x, \widetilde{\Delta}_y)|/\sqrt{2}$. Table 1 lists the rms values for the magnitudes of the (normalized) changes of the vertical and horizontal magnetic field components. The normalized changes tend to be larger in weak field regions, i.e., outside of the AR core (see Figures 1(c) and (d)).

Figure 2(a) shows the mean current-weighted angle for SERIES I (gray stars), with a median of $\theta_J = 9°\!.8 \pm 1°\!.5$. For the volume-averaged fractional flux (black triangles), we find a median value of $\langle|f_i|\rangle \times 10^4 = 13.3 \pm 2.5$. Figure 2(c) shows that $E_{\rm div}/E \gtrsim 0.05$, with a median value of $E_{\rm div}/E = 0.06 \pm 0.02$, for the majority of time instances considered. For SERIES II, we find the median values $\theta_J = 15°\!.6 \pm 2°\!.7$ and $\langle|f_i|\rangle \times 10^4 = 2.2 \pm 1.0$. The nonsolenoidal contribution to the total energy is considerably lower than in SERIES I (Figure 2(d)), with a median value $E_{\rm div}/E = 0.005 \pm 0.003$. Note that the improved solenoidal
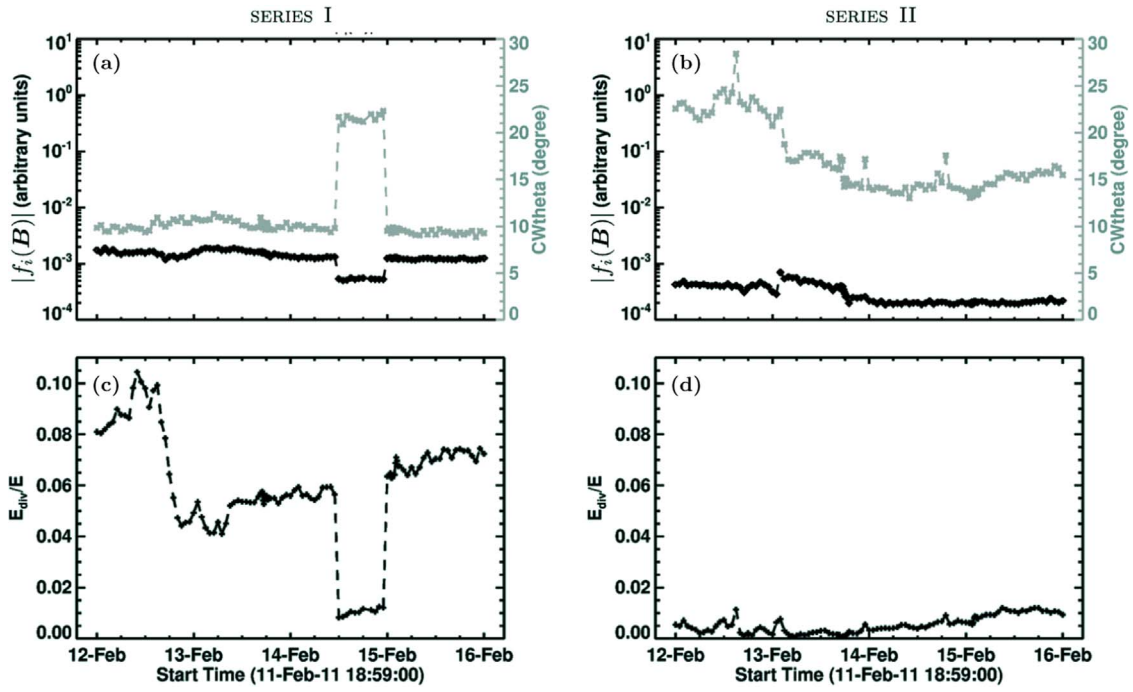
Figure 2. Quality of NLFF magnetic fields of SERIES I (left panels) and SERIES II (right panels). θ_J (gray stars) in panels (a) and (b) quantifies the degree of force-freeness. The fractional flux, $\langle|f_i|\rangle$ (black triangles), quantifies the level of $\nabla \cdot \boldsymbol{B}$. The nonsolenoidal contribution, E_{div}, to the total energy is shown in panels (c) and (d).
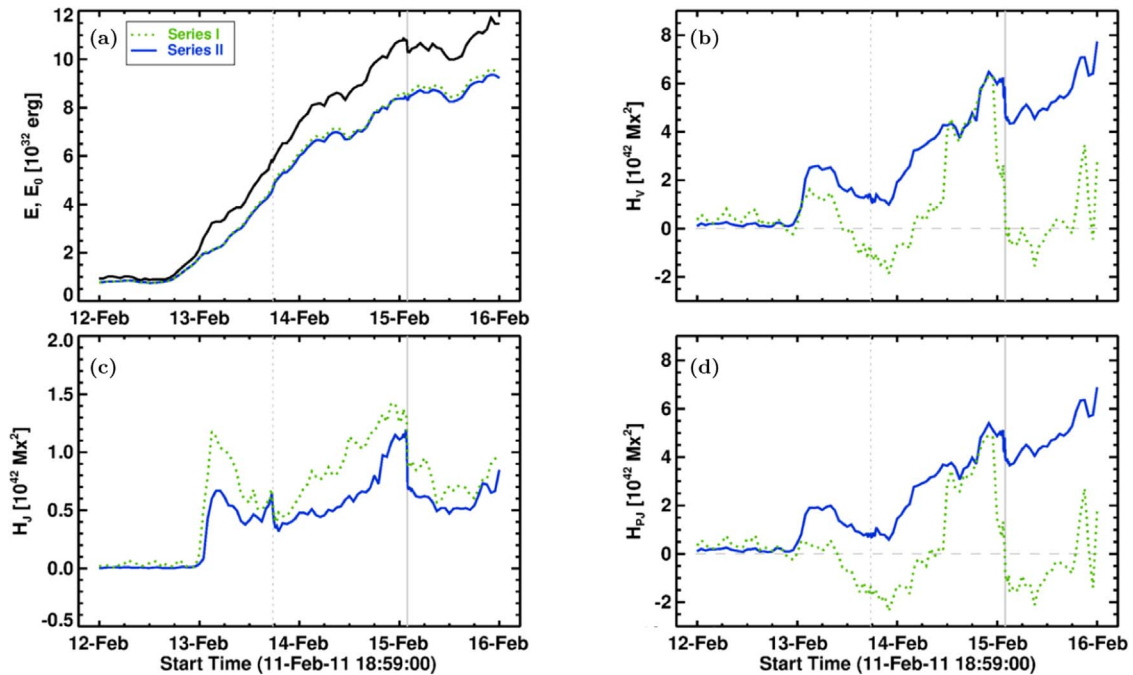

Figure 3. (a) Total energy (E; black solid line) and potential energy (E_0) for SERIES I (green dashed) and SERIES II (blue solid). Panel (b) shows the corresponding total helicity, H_V, derived using the FV$_{\mathrm{Coulomb}}$ method. In panels (c) and (d), the contributions of H_J and H_{PJ} are shown, respectively. Vertical dashed and solid lines mark the *GOES* peak time of M- and X-class flares, respectively.

condition in SERIES II is achieved at the slight expense of force-freeness.

3.2. Effect of Divergence on Helicity Computations

Fast-evolving NOAA 11158 showed a considerable increase of unsigned magnetic flux starting on late February 12, at a time when a pronounced filament started to emerge (for an in-depth analysis see Sun et al. 2012). Parts of the filament erupted during two eruptive flares, an M6.6 flare (SOL2011-02-13T17:38) and an X2.2 flare (SOL2011-02-15T01:56). Figure 3(a) shows the corresponding total (E; black solid line) and potential field (E_0) energy for SERIES I (green dotted line) and SERIES II (blue solid line), including a considerable increase, starting with the emergence of the filament early on February 13.
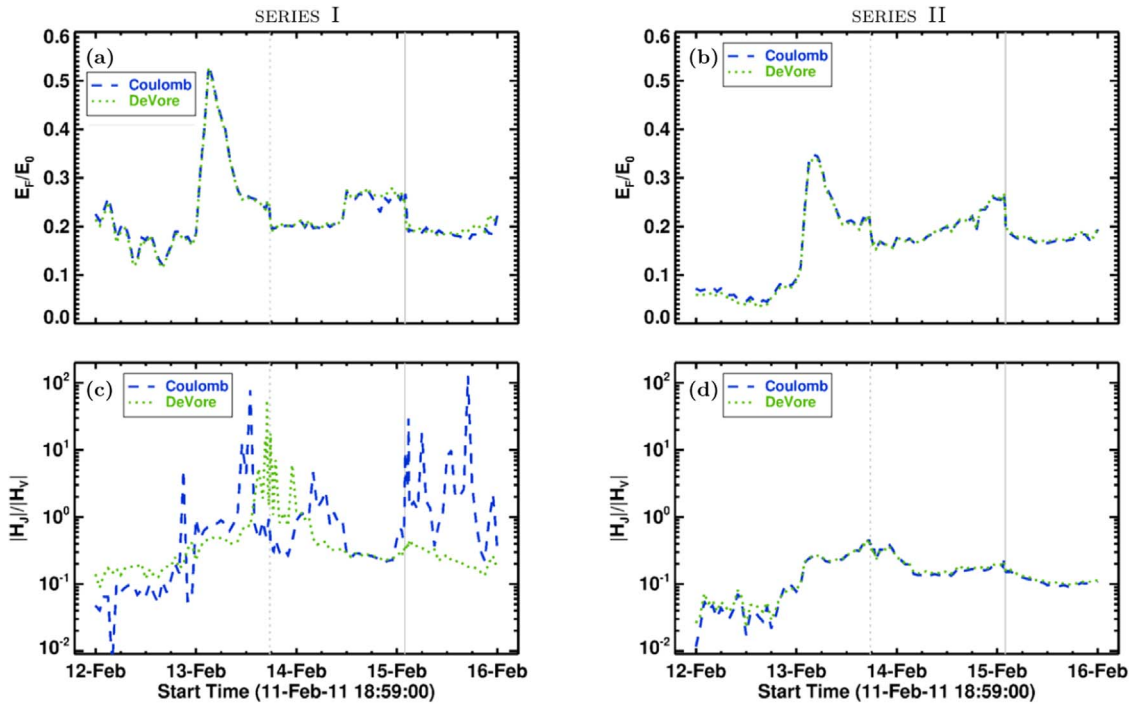
Figure 4. Magnetic energy ratio, E_F/E_0, for (a) SERIES I and (b) SERIES II. Panels (c) and (d) show the helicity ratio, $|H_J|/|H_\mathcal{V}|$, respectively. Blue dashed and green dotted lines represent the model solutions based on the $FV_{Coulomb}$ and FV_{DeVore} methods. Vertical dashed and solid lines mark the *GOES* peak time of M- and X-class flares, respectively.

Figure 3(b) shows the total helicity, $H_\mathcal{V}$, computed with the $FV_{Coulomb}$ method. While exclusively positive values are found for $H_\mathcal{V}$ when based on SERIES II, the corresponding curve of SERIES I shows an unexpected behavior, including rapid and drastic changes, independent of the occurrence of the eruptive flares. A closer look into the contributors to the total helicity, H_J (Figure 3(c)) and H_{PJ} (Figure 3(d)), reveals that these changes mainly stem from the contribution of H_{PJ}. The magnitudes of H_J differ less, with slightly lower values obtained from SERIES II.

Though not shown explicitly, we note that the results derived using the FV_{DeVore} method show a similar behavior, though slightly less extreme. In SERIES I, a good match of $H_\mathcal{V}$ (and thus H_{PJ}) between the two methods is only found during a short time interval, between February 14 ∼12:00 UT and early February 15, i.e., where the input magnetic fields were more divergence-free ($\langle|f_i|\rangle \propto 10^{-4}$ and $E_{div}/E \simeq 0.01$) than at other times (compare Figure 2(c)). In contrast, $FV_{Coulomb}$ and FV_{DeVore} deliver almost identical results for the entire SERIES II.

3.3. Effect of Divergence onto Eruptivity Proxies

Often employed are proxies quantifying the nonpotentiality and eruptivity in the form of the free energy ratio, E_F/E_0, and the helicity ratio, $|H_J|/|H_\mathcal{V}|$. In Figure 4, we compare the effect of divergence in SERIES I (left panels) and SERIES II (right panels) onto the corresponding values derived with the $FV_{Coulomb}$ and FV_{DeVore} method.

While E_F/E_0 is growing prior to the eruptive flares and $\gtrsim 0.2$ in SERIES II (Figure 4(b)), this is not the case for SERIES I (Figure 4(a)). Also, in SERIES I, E_F/E_0 appears rather large prior to the presence of strong magnetic fluxes (before late February 12) at a time when the AR did not exhibit signatures of a filament. Thus, the energy (ratio) at those times is mostly

dominated by the level of $\nabla \cdot \boldsymbol{B}$, and in that sense indicates that anything below $E_F/E_0 \simeq 0.2$ is not significant.

The effect on the helicity ratio $|H_J|/|H_\mathcal{V}|$ is equally severe. While it may serve as a proxy for eruptivity, with (increasing) decreasing trend (before) after the major flares in SERIES II, and values $|H_J|/|H_\mathcal{V}| \gtrsim 0.2$ prior to flare occurrence (Figure 4(d)), such a conclusion cannot be drawn based on SERIES I (Figure 4(c)). Here, clear and smooth trends around flares are hard to discriminate. In particular, $|H_J|/|H_\mathcal{V}|$ exceeds a value of one at times when H_{PJ} based on the respective method takes unexpected turns (compare the dashed blue line in Figure 4(c) and the green dotted line in Figure 3(e) for the $FV_{Coulomb}$ method). Again, $|H_J|/|H_\mathcal{V}|$ based on the two different methods agrees only for times in SERIES I when the underlying magnetic field is more divergence free (compare Figures 2(a) and (c)).

4. Summary and Discussion

We aimed at testing the sensitivity of magnetic energy and helicity computations, based on real solar observations, in terms of the quality of the employed coronal magnetic field model. We employed the method of Wiegelmann & Inhester (2010) based on two different free model parameter sets to a time series of observed vector magnetograms, in order to obtain two time series of NLFF models (SERIES I and SERIES II). A high degree of force-freeness is crucial for the validity of an NLFF solution with respect to the measured photospheric field it is based on. A low level of divergence is mandatory for a reliable computation of magnetic helicity (Valori et al. 2013, 2016).

While the NLFF fields of SERIES I are of "standard" quality ($\theta_J \simeq 10°$, $\langle|f_i|\rangle \propto 10^{-3}$, and $E_{div}/E \gtrsim 0.05$), those of SER-IES II are of higher solenoidal quality ($\langle|f_i|\rangle \propto 10^{-4}$ and $E_{div}/E \simeq 0.01$) and slightly lower force-freeness (Figure 2). The numbers for SERIES II represent remarkably good values

for observation-based NLFF modeling, competing with the best-performing models discussed in DeRosa et al. (2015), while better preserving the original input vector magnetic field (compare the rms values in Tables 1 and 3 of DeRosa et al. 2015).

We applied two different FV methods to compute the magnetic helicity of Thalmann et al. (2011; "FV$_{\rm Coulomb}$") and Valori et al. (2012; "FV$_{\rm DeVore}$"), which are based on different gauges (Coulomb versus DeVore, respectively) and employ different mathematical approaches (differential versus integral formulation for the vector potentials, respectively). We applied both methods to both NLFF time series and find that the different methods deliver almost identical results (i.e., $H_\mathcal{V}$, as well as H_J and $H_{\rm PJ}$), given a sufficient solenoidal quality of the input magnetic field. We therefore suggest that, quite generally, helicity computations may be meaningful and trustworthy only if $E_{\rm div}/E \lesssim 0.05$ and $\langle|f_i|\rangle \times 10^4 \lesssim 5$ for the underlying magnetic field model.

The different methods react differently on the quality of the input fields, with FV$_{\rm Coulomb}$ being more sensitive, with larger absolute variations in $H_{\rm PJ}$ (Figure 3(d)), and hence $H_\mathcal{V}$ (Figure 3(b)). The least difference, even for nonnegligible divergence, is found for H_J, both between the methods and between the two NLFF series (Figure 3(c)), which seems to point to an inconsistency in context with the potential field. In comparison, the magnetic energy shows only little sensitivity to the quality of the underlying NLFF solution (Figure 3(a)). Irrespective of the method, the proxies for nonpotentiality, $E_{\rm F}/E_0$, and for eruptivity, $|H_J|/|H_\mathcal{V}|$, are affected to a degree that allows reliable conclusions only if the input NLFF field is solenoidal enough (Figure 4).

In our case, the unexpected behavior of $H_{\rm PJ}$ (and thus $H_\mathcal{V}$) in SERIES I is caused by a too large divergence of the underlying NLFF solutions ($\langle|f_i|\rangle \times 10^4 \gtrsim 5$ and $E_{\rm div}/E \gtrsim 0.05$). Correspondingly, we are able to verify the doubts of Moraitis et al. (2014) concerning the reliability of their long-term helicity analysis of ARs NOAA 11072 ($\langle|f_i|\rangle \times 10^3 = 1.3 \pm 0.2$) and NOAA 11158 ($\langle|f_i|\rangle \times 10^4 = 7.2 \pm 0.9$). Corresponding judgment of other earlier works are difficult because relevant control parameters were not reported (e.g., Jing et al. 2012, 2015).

The effect of nonsolenoidal contributions to $H_\mathcal{V}$ may be case dependent, however. A similar behavior may in some cases just represent the correct evolution. For instance, the most eruptive case of MHD simulations analyzed in Pariat et al. (2017) shows a change of the sign of $H_{\rm PJ}$, though smoothly and to values small compared to the pre-eruption value. Also, a variation of the sign of H_J around zero, around times when strong magnetic flux is initially emerging in an AR, may just be physical (compare Figures 3 and 6 of Pariat et al. 2017).

In summary, we find that a quantitative assessment of the consistency of NLFF models in terms of force- and divergence-freeness is mandatory for making any reliable statement involving their energy and helicity content. Moreover, despite the necessity of high-quality (i.e., low-divergence) input magnetic fields for helicity computation, simplistic interpretations of the computed magnetic helicity of complex magnetic systems should be taken with care.

ORCID iDs

Julia K. Thalmann ⓘ https://orcid.org/0000-0001-8985-2549
E. Pariat ⓘ https://orcid.org/0000-0002-2900-0608
G. Valori ⓘ https://orcid.org/0000-0001-7809-0067

References

Berger, M. A. 1999, PPCF, 41, B167
Berger, M. A., & Field, G. B. 1984, JFM, 147, 133
Bobra, M. G., Sun, X., Hoeksema, J. T., et al. 2014, SoPh, 289, 3549
DeRosa, M. L., Wheatland, M. S., Leka, K. D., et al. 2015, ApJ, 811, 107
Finn, J., & Antonsen, T. J. 1984, PPCF, 9, 111
Hoeksema, J. T., Liu, Y., Hayashi, K., et al. 2014, SoPh, 289, 3483
Inoue, S., Hayashi, K., Shiota, D., Magara, T., & Choe, G. S. 2013, ApJ, 770, 79
Jing, J., Park, S.-H., Liu, C., et al. 2012, ApJL, 752, L9
Jing, J., Xu, Y., Lee, J., et al. 2015, RAA, 15, 1537
Leka, K. D., Barnes, G., Crouch, A. D., et al. 2009, SoPh, 260, 83
Metcalf, T. R. 1994, SoPh, 155, 235
Moraitis, K., Tziotziou, K., Georgoulis, M. K., & Archontis, V. 2014, SoPh, 289, 4453
Pariat, E., Leake, J. E., Valori, G., et al. 2017, A&A, 601, A125
Pesnell, W. D., Thompson, B. J., & Chamberlin, P. C. 2012, SoPh, 275, 3
Prior, C., & Yeates, A. R. 2014, ApJ, 787, 100
Schou, J., Scherrer, P. H., Bush, R. I., et al. 2012, SoPh, 275, 229
Schrijver, C. J., De Rosa, M. L., Metcalf, T. R., et al. 2006, SoPh, 235, 161
Sun, X., Hoeksema, J. T., Liu, Y., et al. 2012, ApJ, 748, 77
Thalmann, J. K., Inhester, B., & Wiegelmann, T. 2011, SoPh, 272, 243
Valori, G., Démoulin, P., & Pariat, E. 2012, SoPh, 278, 347
Valori, G., Démoulin, P., Pariat, E., & Masson, S. 2013, A&A, 553, A38
Valori, G., Pariat, E., Anfinogentov, S., et al. 2016, SSRv, 201, 147
Wheatland, M. S., Sturrock, P. A., & Roumeliotis, G. 2000, ApJ, 540, 1150
Wiegelmann, T., & Inhester, B. 2010, A&A, 516, A107
Wiegelmann, T., Inhester, B., & Sakurai, T. 2006, SoPh, 233, 215